Dalton Transactions

PAPER

Cite this: *Dalton Trans.*, 2014, **43**, 3626

Evaluation of nickel ferrite nanoparticles coated with oleylamine by NMR relaxation measurements and magnetic hyperthermia†

M. Menelaou,[a] K. Georgoula,[a] K. Simeonidis[b] and C. Dendrinou-Samara*[a]

Received 11th October 2013,
Accepted 17th December 2013

DOI: 10.1039/c3dt52860j

www.rsc.org/dalton

Nickel ferrite nanoparticles were synthesized *via* a facile solvothermal approach. Oleylamine (OAm) was used in all synthetic procedures as a stabilizing agent and solvent. By varying the polarity of the solvents, hydrophobic $NiFe_2O_4$ nanoparticles coated with OAm of relatively similar sizes (9–11.7 nm) and in a range of magnetization values (32.0–53.5 emu g^{-1}) were obtained. The as-prepared hydrophobic nanoparticles were characterized by XRD, TEM, SEM, TGA and VSM and converted to hydrophilic by two different approaches. The addition of a positively charged ligand (cetyltrimethyl ammonium bromide, CTAB) and the ligand exchange procedure (2,3-dimercaptosuccinic acid, DMSA) have been successfully applied. The aqueous suspensions of $NiFe_2O_4$@CTAB and $NiFe_2O_4$@DMSA showed good colloidal stability after a long period of time. The different surface modification affected both the NMR relaxometric measurements and the hyperthermia effects. In both techniques CTAB modification demonstrated higher r_2 relaxivity (278.9 s^{-1} mM^{-1} in an NMR spectrometer at 11.7 T) and SAR values (423.4 W g^{-1} at an applied AC field with a particle concentration of 0.5 mg mL^{-1}). The results indicate that a coating with a larger molecule as CTAB under the same size, shape and magnetization of $NiFe_2O_4$ NPs gave rise to NMR relaxometric properties and heating efficacy.

1. Introduction

Spinel ferrite nanoparticles MFe_2O_4 (where M^{II} = Fe(II), Mn(II), Co(II), Ni(II)) are currently considered among the most successful magnetic nanoparticles (MNPs) for technological and medical applications, spanning from magnetic storage systems,[1] photomagnetic materials,[2] and contrast enhancement in magnetic resonance imaging (MRI)[3] to site-specific drug delivery[4] and hyperthermia.[5] The composition of ferrites depends on the chemical identity of the divalent metal (M^{II}) as well as on the charge and distribution of the metal ions among tetrahedral and octahedral sites of the generic spinel structure. Therefore, it is possible to fabricate ferrites over a continuous range of composition, with completely different magnetic and physicochemical properties and as a consequence different potential applications.[6]

Increased magnetization of MNPs is a matter of concern for all the above applications. Several synthetic procedures are applied to isolate monodispersed ferrite nanoparticles of controllable size and shape targeting to enhanced magnetic properties. A metal dopant substitution strategy of metal ferrite, such as Zn^{2+} dopants, can affect drastically the antiferromagnetic coupling interactions between tetrahedral and octahedral interstices and have been pursued to achieve high and tunable nanomagnetism.[7] It is well known also that the surface organic coating used for the isolation of distinct MNPs and/or for further functionalization may strongly affect the magnetic properties of the nanoparticles through modifying surface spin disorders. π-Acceptors such as oleic acid induce a dramatic collapse of the saturation magnetization; in contrast, σ-donors such as amine ligands increase the spin–orbit coupling due to a decrease of the crystal field splitting and therefore favor the uplift of the magnetocrystalline anisotropy of the surface layer.[8,9] Moreover, it has been demonstrated that increment in magnetization of metal ferrites can be effectively modulated by adsorbed ligands as effectively taking the positions of the missing oxygen atoms resulting in a reduced surface anisotropy.[9,10] Recently, our group demonstrated that high magnetization can be achieved through the control of the composition of the spinel ferrite targeting increased iron content.[11] The effective control of magnetization for the

[a]*Department of Chemistry, Aristotle University of Thessaloniki, 54124 Thessaloniki, Greece. E-mail: samkat@chem.auth.gr; Fax: +30-2310-997738; Tel: +30-2310-997876*

[b]*Department of Mechanical Engineering, School of Engineering, University of Thessaly, 38334 Volos, Greece*

†Electronic supplementary information (ESI) available. See DOI: 10.1039/c3dt52860j

development of applications in the nano regime still remains challenging due to the complexity of the parameters involved.

$NiFe_2O_4$ is a soft magnetic n-type semiconducting material with low magnetic coercivity and high electrical resistivity which possesses a fully inverse structure (i = 1) due to the chemical nature of Ni(II) where all nickel ions are only located in the octahedral sites while iron ions occupy tetrahedral and octahedral sites.[12,13] In particular, $NiFe_2O_4$ nanoparticles have been isolated following synthetic procedures such as thermal decomposition,[14] hydrothermal synthesis,[15] solvothermal synthesis,[16] sol–gel,[17] co-precipitation,[18] combustion reaction,[19] spray-pyrolysis[20] and sol–gel auto-combustion.[21] As a result, most of the applicable techniques lead to hydrophobic $NiFe_2O_4$ nanoparticles in a range of shapes and sizes where coercivity and magnetization values are directly influenced.[16b] Superparamagnetic behavior has been observed as well as the reduction of the saturation magnetization in comparison with the corresponding bulk material (55 emu g^{-1}).[22] The use of such nanoparticles for new biomedical applications requires aqueous dispersion and further functionalization. In this case, tailoring the surface and understanding the surface characteristics are necessary.

The present work deals with the preparation and the study of the magnetic properties of $NiFe_2O_4$ nanoparticles *via* a solvothermal procedure as well as the evaluation of the nanoparticles as potential T_2 MRI contrast agents and hyperthermia heating mediators. In the first step, the relationship between the synthesis and the magnetic properties was investigated. In so doing, we select all preparations to take place at 200 °C in the presence of a σ-donor, oleylamine, while by varying the polarity of the solvents, nickel ferrite nanoparticles of similar sizes with different magnetization are isolated. The structure and morphology were characterized by XRD, SEM and TEM while the magnetic properties were measured by VSM. To the best of our knowledge, there is no previous report on how oleylamine acts as a sole surfactant and/or in a triple role (surfactant/solvent/reducing agent) through solvothermal synthesis of $NiFe_2O_4$ nanoparticles. In a second step, the hydrophobic $NiFe_2O_4$ nanoparticles were converted to hydrophilic by two different approaches to study the effect of surface modification: (i) by addition of a positively charged ligand cetyltrimethyl ammonium bromide (CTAB) and (ii) by the ligand exchange procedure in the presence of 2,3-dimercaptosuccinic acid (DMSA). Moreover, the resulting hydrophilic $NiFe_2O_4$ nanoparticles of both approaches were evaluated using NMR relaxation measurements while their magnetic hyperthermia effects were also studied and their characteristics are discussed.

2. Experimental section

Materials

All the reagents were of analytical grade and were used without any further purification. Iron(III) acetylacetonate $Fe(acac)_3$ (≥97.0%) was purchased from Fluka. Oleylamine (OAm) of technical grade (70.0%), dimethylsulfoxide (DMSO), diphenyl ether (≥99%) and NaOH pellets were purchased from Sigma-Aldrich. Nickel(II) acetylacetonate $Ni(acac)_2$ (≥99.9%) was purchased from Riedel-de Haën and hydrazine hydrate $N_2H_4{\cdot}H_2O$ from Merck. *meso*-2,3-Dimercaptosuccinic acid (DMSA) was purchased from Tokyo Chemical Industry (TCI) Co. Ltd. Cetyltrimethyl ammonium bromide (CTAB) (98.0%) was purchased from Alfa Aesar, A Johnson Matthey Company. Deuterium oxide (D_2O) (99.9%) was purchased from Deutero GmbH. All aqueous solutions were prepared with water from a Milli-Q water purification system.

Synthesis of the $NiFe_2O_4$ nanoparticles

A general synthetic procedure for the preparation of the MNPs was carried out in air in which $Fe(acac)_3$ (1.8 mmol, 0.636 g) and $Ni(acac)_2$ (0.9 mmol, 0.232 g) were mixed only with oleylamine (14 mL) acting as both a surfactant and a solvent. The resulting solution was stirred thoroughly for 15 min and then transferred into a 23 mL Teflon-lined stainless-steel autoclave and was heated up with a stable rate of 4 °C min^{-1} until the temperature reached 200 °C while it remained stable for 24 h. After a 24 h reaction, the Teflon lined bombs were left to cool down to room temperature at a stable rate of 5 °C min^{-1} and then centrifuged at 1000 rpm. The supernatant liquid was discarded and a black-brown precipitate was obtained. The precipitate was washed with ethanol for at least three times in order to remove any excess of oleylamine and unreacted precursors.

The above procedure was followed for the isolation of sample D1. A number of modifications were applied then for the rest of the samples; keeping the same metal ratio (Ni : Fe 1 : 2) and the total volume of the surfactant/solvent (14 mL) constant, solvents with different polarities were used. For sample D2, the metal precursors were mixed and dissolved in a mixture of oleylamine (4 mL) and diphenyl ether (9 mL). Following the synthetic conditions for D2, hydrazine (44 μL) was also added in the presence of 9 mL of diphenyl ether to prepare sample D3. Finally, for sample D4, water was used as a solvent (9 mL). Table 1 summarizes the synthetic conditions for all obtained samples.

Surface modification methods

Method A. Surface modification of $NiFe_2O_4$ NPs *via* CTAB. The as-prepared hydrophobic $NiFe_2O_4$ NPs (samples D1, D2 and D3) were converted to hydrophilic *via* the cationic

Table 1 Synthetic conditions for the isolation of $NiFe_2O_4$ nanoparticles

Sample	Phase	Molar ratio (Ni : Fe)	Surfactant	Solvent	Reducing agent
D1	$NiFe_2O_4$	1 : 2	OAm[a]	OAm	OAm
D2	$NiFe_2O_4$	1 : 2	OAm	OAm/ DPHE[b]	OAm
D3	$NiFe_2O_4$	1 : 2	OAm	OAm/ DPHE	OAm/ Hydrazine
D4	$NiFe_2O_4$	1 : 2	OAm	OAm/H_2O	OAm

[a] Oleylamine. [b] Diphenyl ether.

surfactant cetyltrimethyl ammonium bromide ($CH_3(CH_2)_{15}N^+(CH_3)_3Br^-$ (CTAB)) according to a previously reported method.[23] 0.02 M CTAB was added to ultrapure water to form solution A. Then, 3 mg of samples D1, D2 and D3, respectively, were dispersed in 0.5 mL of chloroform to form solution B. Solutions A and B were mixed together to generate an oil-in-water microemulsion and the mixture was sonicated for more than 5 h until the chloroform was completely evaporated, leaving an orange-brown aqueous solution. The resulting suspensions are stable in water for a long period and are named as D1@CTAB, D2@CTAB and D3@CTAB, respectively.

Method B. Surface modification of $NiFe_2O_4$ NPs *via* surface exchange (DMSA). A mixture of 10 mg of *meso*-2,3-dimercaptosuccinic acid (DMSA) in 0.5 mL of dimethyl sulfoxide (DMSO) was added to a mixture of 10 mg of $NiFe_2O_4$ NPs (samples D1 and D2) in 3 mL of toluene. The resulting mixture was sonicated for 2 hours and mechanically stirred for 24 hours at room temperature. After that, the supernatant was discarded. The precipitated $NiFe_2O_4$@DMSA NPs were successfully mixed and centrifuged with ethanol several times to remove free oleylamine molecules before being dispersed in water. The pH of aqueous suspension increased to 10 with 1 M NaOH solution in order to deprotonate the carboxylic groups and thiol groups (p*K* 9.2) of the DMSA.[24] Finally, the pH was adjusted to 7 with the addition of 1 M HNO_3 solution in order to achieve better dispersion of the ferrite NPs.[24,25] The resulting suspensions are stable in water for a prolonged period and are named as D1@DMSA and D2@DMSA.

Physical measurements and characterization techniques

X-ray powder diffraction (XRD) measurements were performed on phase identification using a 2-cycle Rigaku Ultima diffractometer (40 kV, 30 mA) with monochromatized Cu Kα radiation (λ = 1.5406 nm) with Bragg–Brentano geometry (detection limit approximately 2%). Conventional TEM images were obtained using a JEOL 100 CX microscope (TEM) operating at an acceleration voltage of 100 kV. For TEM observations we have used suspensions of the nanoparticles in organic solvents (toluene or chloroform) deposited onto carbon-coated copper TEM grids. The elemental composition of the samples was tested by inductively coupled plasma atomic emission spectroscopy (ICP-AES), Perkin-Elmer Optima 3100XL, by scanning electron microscopy (SEM), JEOL 840A, and a flame atomic absorption spectrometer (FAAS), AAnalyst 400, Perkin Elmer. Fourier-Transform Infrared Spectroscopy was recorded using a Nicolet FTIR 6700 spectrometer with KBr pellets in the range 350–4000 cm^{-1}. Thermogravimetric analysis (TGA) was performed using SETA-RAM SetSys-1200 and carried out in the range from room temperature to 850 °C at a heating rate of 10 °C min^{-1} under an N_2 atmosphere. Magnetic measurements were performed at 300 K using a 1.2 H/CF/HT Oxford Instruments VSM. The AC thermal response of the samples was measured at 765 kHz by recording the temperature rise with an OpSensPicoM optic fiber thermometer in an AC field (250 Oe) application.

NMR relaxation measurements

The spin–spin T_2 relaxation times of hydrogen protons in ultrapure water and 10% D_2O at various concentrations of the modified nanoparticles ranging from 0.2 to 0.8 mM were determined using an 11.7 T NMR spectrometer (Agilent 500 MHz) at 20 °C. T_2 was acquired using the Carr-Purcell-Meiboon-Gill (CPMG) pulse sequence. T_2 analysis in order to fit the data for the T_2 curves for each peak was performed *via* the VNMRJ 3.1 software.

Magnetic hyperthermia

A test tube containing 1 mL of the suspension in various concentrations of each sample (0.5 mg mL^{-1}, 1 mg mL^{-1} and 2 mg mL^{-1}) was placed in the center of a water-cooled induction coil with 23 mm diameter consisting of three turns and connected to an AC field generator of 4.5 kW.

3. Results and discussion

Synthetic aspects

$NiFe_2O_4$ nanoparticles were synthesized *via* solvothermal synthesis as a simple, eco-friendly and cost effective way to afford high crystallinity materials.[16] The reaction conditions are easily reproducible and can be further scaled up for mass production.

OAm has been selected for the synthesis based on its multifunctional role: it is a long chain primary alkylamine which acts as a mild reducing agent; it is liquid in room temperature with a high boiling point (348–350 °C) that allows a high temperature wet route to be carried out; it disperses in various organic solvents and is manipulated easily through the washing procedures that follow for the separation of the NPs; moreover it exhibits σ-donor affinity and increases the spin–orbit coupling as it decreases the crystal field splitting and therefore favors the increment of the magnetocrystalline anisotropy of the surface layer. The role of OAm in nanoparticle synthesis has been recently reviewed and all the important aspects in the formation of noble metal NPs, semiconductors and transition metal oxide NPs through different synthetic methods were illustrated.[26] Nevertheless, OAm has scarcely been reported until now in a multiple role in the synthesis of MFe_2O_4 NPs; two recent reports are referenced for M = Co, Mn, Cu and Zn, where it has been used through a thermal decomposition preparation.[14,27] Very often, *via* a variety of synthetic routes, nanoparticles are stabilized through a mixture of OAm and oleic acid (OA).[28] In the present study, OAm was employed in a triple role (sample D1) while in the presence of a high boiling point non-polar solvent such as diphenylether (sample D2), OAm acts as a typical surfactant. The presence of an extra reducing agent, *e.g.* hydrazine, was examined (sample D3) since in some cases it has been stated that the shape of NPs is influenced by the presence of reductants.[29] Finally, water was employed in the preparation of sample D4, and in this regard, water-in-oil microemulsions were formed by well-defined nanodroplets present in the aqueous phase and

dispersed by the assembly of surfactant molecules in a continuous oil phase.[30] Therefore, the impact of the solvent on the composition of $NiFe_2O_4$ nanoparticles was explored while the rest of the synthetic parameters remained constant.

Structural and magnetic characterization

The XRD patterns for the prepared samples are illustrated in Fig. 1. The spectra exhibit Bragg reflections which are typical of the inverse spinel structure, with relatively broad peaks due to the small size of the crystalline domains. The position and relative intensity of the diffraction peaks provided clear evidence for the formation of pure inverse spinel and face centered cubic (fcc) structure of single-phase nickel ferrite with *Fd3m* space group (JCPDS card no. 10-0325) and correspond to the crystal planes (220), (311), (222), (400), (422), (511), and (440).

The XRD patterns of the samples present effective line broadening indicative of the nano sizes. The average crystalline size of the samples has been calculated from the XRD line of the full width at half-maximum (FWHM) of the most intense peak (311) using Scherrer's formula[31] and was found to be 10.0 nm for D1, 9.6 nm for D2, 9.3 nm for D3 and 12.3 nm for D4, respectively. The corresponding values of the lattice parameters for D1–D4 were calculated to be a = 8.414(2) Å, a = 8.407(4) Å, a = 8.382(6) Å and a = 8.373(5) Å, respectively, slightly larger than the bulk $NiFe_2O_4$ (a = 8.339 Å), but in agreement with earlier reported values for $NiFe_2O_4$ NPs.[16b] The observed expansion of the lattice parameter of sample D4 is inversely analogous to the size.[15a] It has to be mentioned also that a higher degree of crystallinity has been observed for sample D4.

Representative transmission electron microscopy (TEM) images together with corresponding particle size distributions are presented in Fig. 2 (samples D1–D4). The sizes of the particles were arithmetically averaged directly (weighting by number). The number-weighted distributions were built by counting ~150 particles for each sample and were fitted with a standard log–normal function. The size of the nanoparticles varies from 9.0 to 11.7 nm, as is presented in Table 2, and these values are close to the corresponding ones from the XRD patterns indicating their single crystal character.

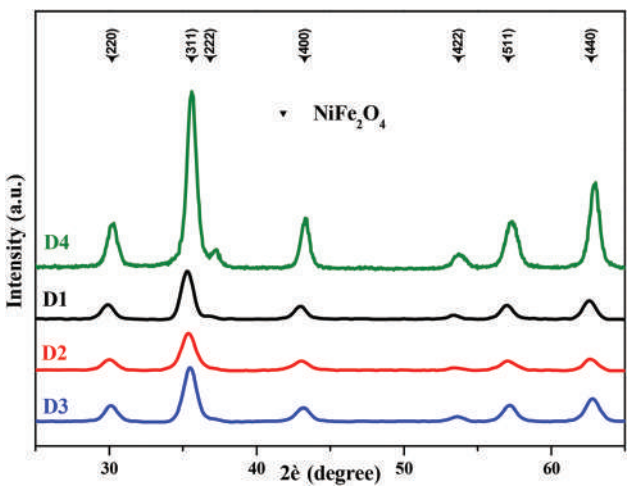

Fig. 1 X-ray diffraction patterns of the nickel ferrite ($NiFe_2O_4$) nanoparticles (samples D1–D4). The data confirm that the nanoparticles are pure phase of spinel nickel ferrite with *Fd3m* space group (JCPDS card no. 10-0325).

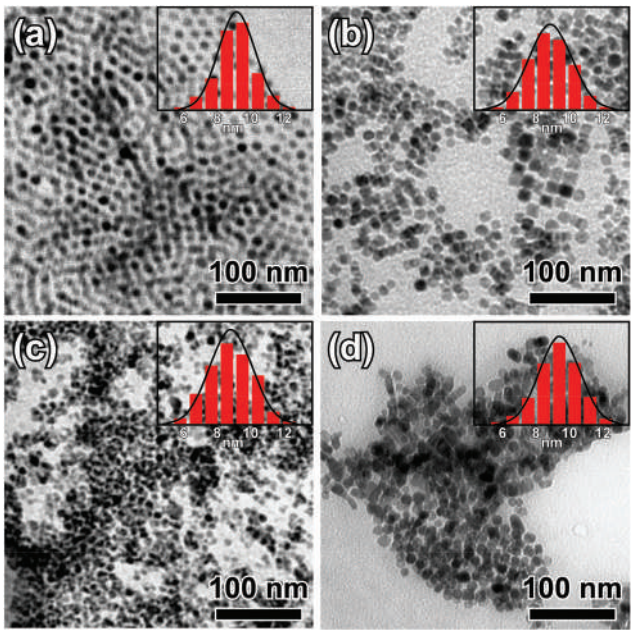

Fig. 2 Representative TEM images and particle size distribution histograms (insets) of samples: (a) D1, (b) D2, (c) D3 and (d) D4.

The size and morphology of the nanoparticles vary depending on the reaction conditions. In particular, when only OAm is present (sample D1) monodispersed almost spherical nanoparticles are displayed. In the presence of the non-polar solvent (samples D2 and D3) truncated nanoparticles of identical mean size are favored while the extra use of the reducing agent (hydrazine) led to lower monodispersity without any shape changes. However, in the presence of water, monodispersed truncated and bigger sizes were formed (sample D4). In general, water has a multiple role since as a chemically active solvent it is involved in each step of the reactions that take place, participates in the acid–base equilibrium as well as in

Table 2 Size, magnetic parameters, relaxivity (r_2) and maximum SAR values of the $NiFe_2O_4$ NPs

Sample	TEM size (nm)	XRD size (nm)	M_s [a] (emu g^{-1}) 300 K	H_c (Oe)	r_2 (s^{-1} mM^{-1})	SAR_{max} (W g^{-1})
D1	9.7 ± 1.3	10.0	50.1	230	220.6	371.7
D2	9.0 ± 1.5	9.6	53.5	182	278.9	423.4
D3	9.0 ± 2.0	9.3	38.8	139	198.2	—
D4	11.7 ± 1.1	12.3	32.0	183	—	—
D1@DMSA			45.0	125	173.7	92.7
D2@DMSA			48.1	163	200.0	125.6

[a] The normalized values of M_s are estimated from the reduced mass of each sample.

the coordination sphere of the metal ions. More important, when water is present as a solvent, a different mechanism occurs where hydrolysis is fast and Fe^{3+} ions are hydrolyzed into $Fe(OH)_3$ and then transformed to β-FeOOH. The composition of $Ni(OH)_2$ occurs in a second step resulting in the final formation of the nickel ferrite as shown in the following reactions:[32]

$$Fe^{3+} + 3OH^- \rightarrow Fe(OH)_3 \quad (1)$$

$$Ni^{2+} + 2OH^- \rightarrow Ni(OH)_2 \quad (2)$$

$$Fe(OH)_3 \rightarrow \beta\text{-}FeOOH + H_2O \quad (3)$$

$$2\beta\text{-}FeOOH + Ni(OH)_2 \rightarrow NiFe_2O_4 + 2H_2O \quad (4)$$

If so, the larger particle size of sample D4 can be ascribed to Ostwald ripening since in a heterogeneous solution (water and OAm) the process reaches a more thermodynamically stable state wherein the surface to area ratio is minimized. Therefore, the growth of larger particles occurs at the expense of less stable smaller particles.[33] This is also confirmed by the different broadening of sample D4 in the XRD patterns, as shown in Fig. 1.

The FT-IR spectra of the $NiFe_2O_4$ NPs in the region 4000–350 cm^{-1} exhibit absorption bands which are in good agreement with the characteristic FT-IR bands of pure oleylamine (Fig. 3).[26] The broad frequency band around ~3500 cm^{-1} is attributed both to the existence of physically absorbed water as well as to the asymmetric (ν_{as}) and symmetric (ν_s) stretching vibrations of the amine groups ($-NH_2$) of the OAm molecule, respectively. The bands observed at ~2921 cm^{-1} and 2853 cm^{-1} are characteristic of the asymmetric (ν_{as}) and symmetric (ν_s) stretching vibrations of methylene groups ($-CH_2$), respectively. The peak at about 1560 is attributed to the NH_2 group and is found to be shifted to some extent, due to interactions with the metal core. For samples D1–D3, a broad shoulder is observed at 1635 cm^{-1} and is attributed to the stretching vibration of the double bond (δ(–C=C)) while in the case of sample D4, the intensity of this peak changed due to different orientation of the double bond[34] since the synthesis was carried out in a water–OAm mixture. Moreover, the peaks below 700 cm^{-1} are assigned to four vibrational modes (ν_1–ν_4) as a result of the specific structure of the prepared nanoparticles.[35] The two modes ν_1 and ν_2 are those with the highest frequencies and are due to the stretching vibration of the tetrahedral and octahedral sites, respectively. The two low-frequency modes, ν_3 and ν_4, can be correlated to oscillations of the metal ions in the isotropic force field of the tetrahedral and octahedral environments, respectively. In our case, ν_1 is obtained at around 605 cm^{-1} and ν_2 is detected at around 410 cm^{-1}. The two lower frequency modes are missing due to the instrument limitations.

The amount of surfactants coated on the surface of the NPs was quantitatively recorded by thermogravimetric analysis (TGA) (Fig. S1, ESI†). The total amount of weight loss of samples D1–D4 is 27.5 wt%, 25.3 wt%, 24.2 wt% and 19.6 wt%, respectively, by measuring the mass reduction in the range of 100–850 °C. The decomposition of the organic coating occurs in a similar way for all samples. Two regions of mass reduction were observed at 100–450 °C and 450–650 °C; in the first step hydrocarbon chains were removed while the nitrogen head groups were burnt off in the second step. This behavior is similar to that reported previously for oleylamine-capped NPs (100–300 °C and 500–700 °C).[36] In accordance with the FT-IR spectra, as nitrogen head groups were coordinated on the NPs surface, they still remained on the surface and decomposed at higher temperature. The relatively lower weight loss in the case of D4 can be explained by the increase of the particle size (D4 found ~12 nm) as the surface area-to-volume ratio is decreased.

Magnetic measurements of the as-prepared nanoparticles were carried out at room temperature using a vibrating sample magnetometer (VSM) with an applied field of 10 kOe. The room temperature hysteresis loops (Fig. 4) for samples D1–D4

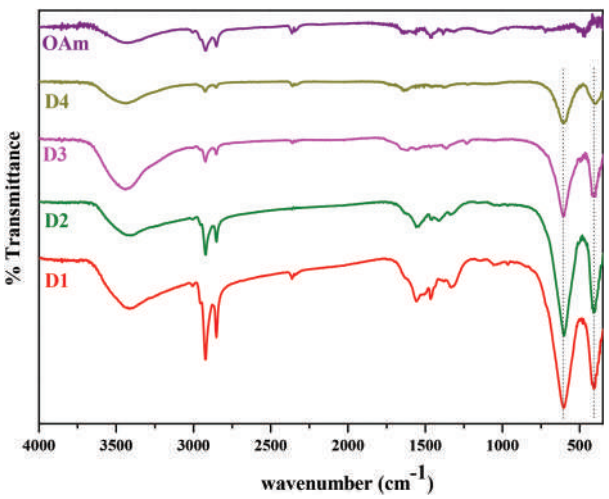

Fig. 3 FT-IR spectra of the OAm ligand and OAm-capped $NiFe_2O_4$ nanoparticles (D1–D4). The dashed lines demonstrate absorption bands of ν_1 and ν_2 modes.

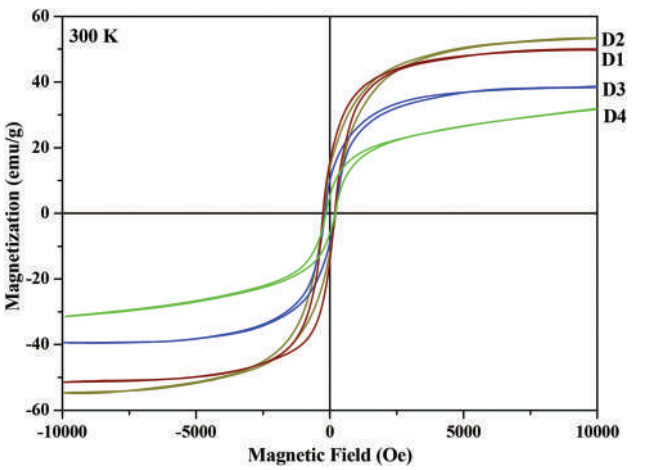

Fig. 4 VSM measurements at 300 K of the effective mass for samples D1–D4.

revealed the characteristic behavior of soft magnetic materials. The saturation magnetization (M_s) values are 38.0 emu g^{-1}, 40.0 emu g^{-1}, 29.0 emu g^{-1} and 25.7 emu g^{-1}, while the normalized values of M_s estimated from the reduced mass of the nanoparticles incorporating the thermogravimetric analysis are 50.1 emu g^{-1}, 53.5 emu g^{-1}, 38.8 emu g^{-1} and 32.0 emu g^{-1} for D1–D4, respectively (Table 2). The resulting values depend significantly on the synthetic route. Enhanced magnetization, close to the bulk (55 emu g^{-1}), is achieved in the presence of the non-polar solvent while in the presence of an extra reducing agent, namely hydrazine, the magnetization is lower due to extra reduction of Fe^{3+} to Fe^{2+} taking into account that crystallinity, particle size and shape are almost the same for samples D1–D3. Divalent iron ions possess $4\mu_B$ and their distribution between A and B sites of the spinel structure led to the observed decline in net magnetization.[37] The lowest magnetization value of sample D4, despite possessing bigger size and higher crystallinity, is attributed to the difference in structural morphology of the spinel due to the participation of water and/or potential surface spin disorder and the existence of a dead magnetic layer.[38]

Surface modification and characterization of the functionalized $NiFe_2O_4$ NPs

The as-prepared hydrophobic NPs were further modified to hydrophilic using two different methods in order to study how different coatings affect NMR relaxivity and hyperthermic effects. The first qualitative method employed a cationic surfactant, CTAB, as a phase transfer agent in water, to create an oil-in-water microemulsion. This interfacial process leads to assembly of surfactant molecules with a positively charged group on the surface of the NPs by compact hydrophobic layers of the outer hydrophobic group of the surfactant molecules and the inner OAm molecules.[23b,39] The second quantitative method was achieved through ligand exchange where a nontoxic substance DMSA, which possesses carboxylic groups, was employed.[40] The modification is carried out in a mixture of DMSO and toluene, which dissolves nicely the DMSA molecules while the hydrophobic particles can be well-dispersed in it. In order to obtain stable and clear dispersion, the pH value has been adjusted in an alkaline environment where negative charge is generated along with the sulfur–sulfur bondings around the particle.[40] It has to be noted here that both procedures were successful since they led to stable colloidal dispersions for at least a period of six months. A schematic illustration of both procedures is given in Scheme 1.

The modified with DMSA nanoparticles have been further characterized since potential changes to the size, shape and composition of the nanoparticles have been reported in some cases.[41] The presence of DMSA on the surface of the NPs was confirmed by FT-IR spectroscopy (Fig. 5a) where a sharp peak at 1704 cm^{-1} is attributed to free carbonyl stretch while two intense peaks at 1577 and 1381 cm^{-1} are assigned to the asymmetric $\nu_{as}(COO^-)$ and symmetric $\nu_s(COO^-)$ carboxylate stretch of DMSA. The difference between these peaks $\Delta(\nu_{as}(COO^-) - \nu_s(COO^-))$ is 196 cm^{-1} and indicated a covalent binding while the splitting of $\nu_{as}(COO^-)$ can be assigned to different

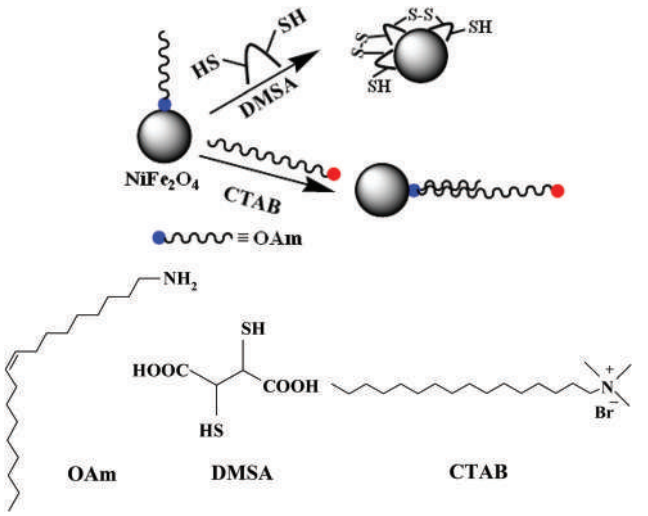

Scheme 1 Schematic illustration of the $NiFe_2O_4$@DMSA and $NiFe_2O_4$@CTAB NPs and chemical structure of the employed molecules (OAm, DMSA, CTAB).

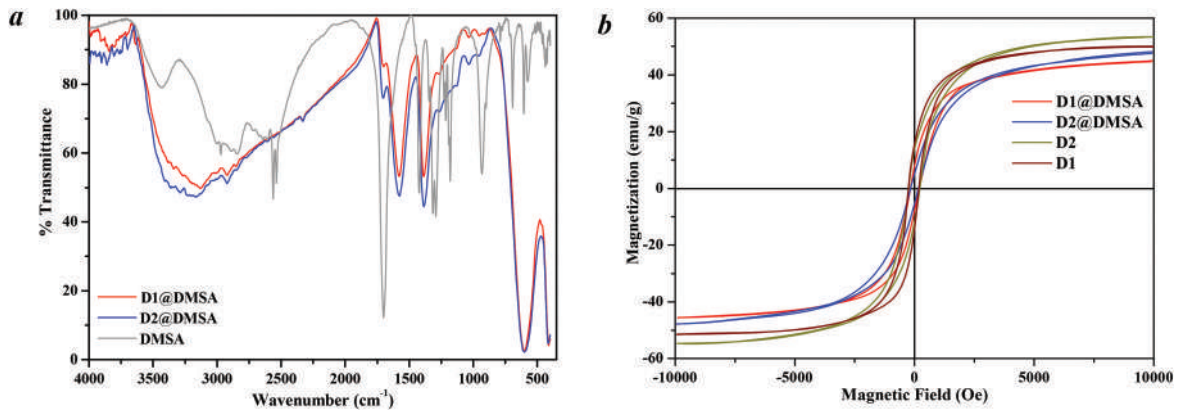

Fig. 5 FTIR spectra of free DMSA and functionalized $NiFe_2O_4$ nanoparticles (D1@DMSA and D2@DMSA) (a) and magnetization curves at 300 K on the effective mass for the as-prepared (D1 and D2) and the functionalized $NiFe_2O_4$ nanoparticles (b).

coordination modes of the carboxyl groups. The peak at ~2520 cm^{-1} present in the spectrum of the free DMSA is assigned to the S–H bond stretching while missing from the spectra of all samples. Also, the composition has proven to be stable for all samples since the Ni/Fe ratio remained constant (1Ni : 2Fe) as shown *via* atomic absorption spectroscopy (FAAS). VSM measurements of D1@DMSA and D2@DMSA in regard to the as prepared NPs D1 and D2 are given in Fig. 5b. The total magnetization remained the same with the as-prepared samples (38 emu g^{-1} and 40 emu g^{-1} for D1@DMSA and D2@DMSA, respectively). Calculation of the organic coating (DMSA) and further correction of the magnetization values showed that the normalized magnetization is 45.0 emu g^{-1} and 48.1 emu g^{-1} for D1@DMSA and D2@DMSA, respectively, since 17% and 18% by weight is attributed to the DMSA ligands. TGA analysis of both samples is given in the ESI (Fig. S2 and S3†). Thus, no aggregation and/or size effect can be stated after the modification and the reduced magnetization is assigned to the less organic coating (27.5 wt% and 25.3 wt% for D1 and D2, respectively).

NMR relaxation measurements

Magnetic resonance imaging (MRI) and nuclear magnetic resonance (NMR) are based on the relaxation process of protons when placed in an external magnetic field.[42] There are two types of relaxation processes: the longitudinal or spin–lattice relaxation process (T_1) and the transverse or spin–spin relaxation process (T_2). T_2 contrast agents are generally based on superparamagnetic nanoparticles. Dextran-coated superparamagnetic iron oxide nanoparticles (SPIO) are already commercially used as T_2 contrast agents for clinical applications.[43] Based on Koenig and Kellar,[44] r_2 relaxivity is proportional to the square of magnetic moment according to the following equation:

$$R_2 = \frac{1}{T_2} = \frac{\alpha}{Dd_{NP}}\gamma^2\mu^2 C_{NP} J(\omega, \tau_D) \quad (5)$$

where α is a constant, D is the diffusion coefficient, d_{NP} is the diameter of the nanoparticle, γ is the gyromagnetic ratio of the water proton, μ is the magnetic moment of the proton, C_{NP} is the concentration of the nanoparticles, and $J(\omega, \tau_D)$ is the spectral density function.

The transverse T_2 (or spin–spin) relaxation times of hydrogen protons of pure water at various concentrations of the samples were determined using an NMR spectrometer. The efficiency of a contrast agent is defined in terms of the transverse (r_2) relaxivity, which corresponds to the rates of proton relaxation and is determined according to the following equation:

$$R_2 = \frac{1}{T_2} = \frac{1}{T_2^0} + r_2[\mathrm{M}] \quad (6)$$

where T_2 is the observed proton relaxation time in the presence of nickel ferrite nanoparticles, T_2^0 is the proton relaxation time of pure water and [M] is the concentration of the contrast agent.

The NMR relaxivity studies were performed on the hydrophilic modified NPs: (i) D1@CTAB, D2@CTAB and D3@CTAB, and (ii) D1@DMSA and D2@DMSA. Fig. 6a and 6b show the plot of the relaxation rate R_2 ($1/T_2$) as a function of the metal ion concentration (Ni + Fe) of all samples. The relaxivity (r_2) for each system was determined by the slope of a straight line connecting the different points in the plot among different concentration values.

The corresponding r_2 relaxivity values for the aqueous suspensions of D1@CTAB, D2@CTAB and D3@CTAB were found to be 220.6, 278.9 and 198.2 s^{-1} mM^{-1}, respectively, while for D1@DMSA and D2@DMSA the values are 173.7 and 200.0 s^{-1} mM^{-1}, respectively (Table 2). The two modification approaches led to different r_2 values with the one for D2@CTAB being ~1.4 times higher than that of D2@DMSA. Relaxivities of the modified NPs (D1@CTAB and D2@CTAB) are comparable and even higher than that of the reported values of γ-Fe_2O_3@SiO_2 NPs studied in a similar NMR spectrometer (11.7 T) where the highest r_2 value is equal to 228 s^{-1} mM^{-1} and corresponds to 10.0 nm γ-Fe_2O_3 nanoparticles.[45] Considering that the $NiFe_2O_4$ NPs have similar sizes and M_s values, the differences are attributed to the larger hydrophilic coating of the CTAB molecule

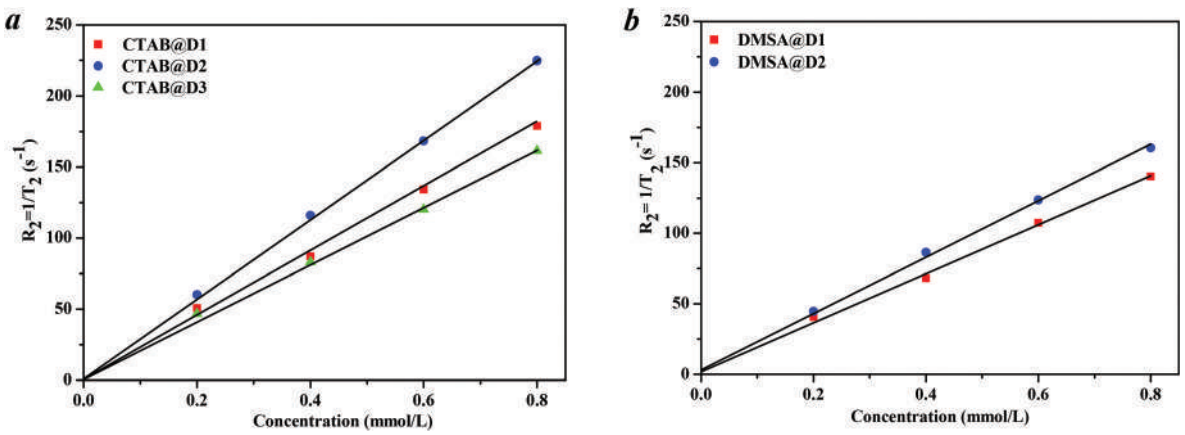

Fig. 6 T_2 Relaxivity plots of aqueous suspensions of $NiFe_2O_4$@CTAB (a) and $NiFe_2O_4$@DMSA (b) nanoparticles.

which favors the diffusion of water molecules unlike the smaller DMSA ligands. Also, "ice-like" water phenomena for the $NiFe_2O_4$@CTAB systems which can induce the r_2 values cannot occur, as has been previously reported in the case of Pluronic F127, most likely due to the smaller size of CTAB molecules. Moreover, the small r_2 values of the $NiFe_2O_4$@DMSA systems suggest that no agglomeration could likely occur.[46]

Magnetic hyperthermia properties

Magnetic nanoparticles such as ferrite nanoparticles have shown promising results as potential heating mediators in magnetic particle hyperthermia due to their efficiency in conversion of magnetic energy into heat even at low concentrations.[47] Thermal activation experiments were performed on the two nickel ferrite nanostructures with the highest magnetization value (D1 and D2) coated either with CTAB or DMSA to determine the specific absorption rate, SAR (W g^{-1}).[48]

SAR demonstrates the heating ability of magnetic materials in the presence of an AC magnetic field and is defined as the amount of heat generated per gram unit of magnetic material per time unit.

$$\mathrm{SAR} = \frac{Cm_s}{m_{NPs}}\left(\frac{dT}{dt}\right) \quad (7)$$

In eqn (7), C is the sample specific heat capacity (C_{water} = 4.186 J g^{-1} C^{-1}), dT/dt is the initial slope of the temperature *versus* time graph, m_s is the mass of the suspension, and m_{NPs} is the mass of the nanoparticles in suspension.[49]

Fig. 7a and 7b show the temperature *versus* time curves for $NiFe_2O_4$@CTAB nanoparticles and $NiFe_2O_4$@DMSA nanoparticles, at three different concentrations varying from 0.5 mg

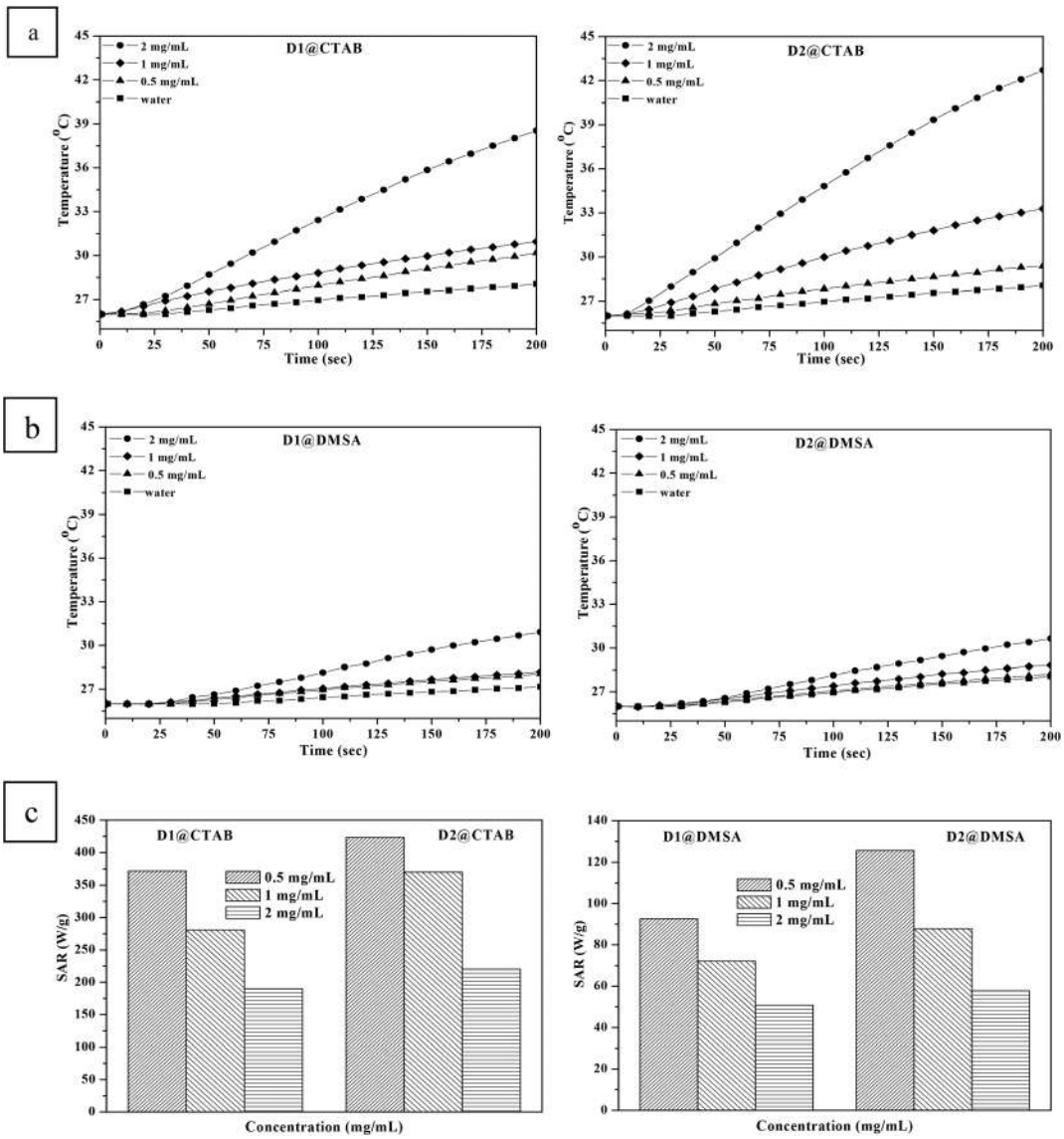

Fig. 7 Temperature *versus* time curve for D1@CTAB and D2@CTAB (a) and D1@DMSA and D2@DMSA (b) $NiFe_2O_4$ nanoparticles. SAR values for $NiFe_2O_4$@CTAB and $NiFe_2O_4$@DMSA (c) systems at various concentrations.

mL^{-1} to 2 mg mL^{-1} in water, respectively. Both graphs indicate a rise in temperature as the concentration increases in the presence of an AC applied field.

SAR values of $NiFe_2O_4$@CTAB and $NiFe_2O_4$@DMSA nanoparticles are calculated from eqn (7) and the initial slope as is demonstrated in Fig. 7a and 7b. We remark that the SAR values were calculated without any organic component correction, since for potential applications, the relevant values are those measured experimentally. As it can be seen from Fig. 7c, SAR values gradually decrease with an increase of the particle concentration (0.5 mg mL^{-1} to 2.0 mg mL^{-1}) in all systems. The maximum SAR value among $NiFe_2O_4$@CTAB systems is 423.4 W g^{-1} while among $NiFe_2O_4$@DMSA systems it is 92.7 W g^{-1}. As the concentration of the particles is increased, the separation between them decreases leading to dipolar interactions and in either ferromagnetic or antiferromagnetic interaction while the heating capacity is decreased. A similar behavior to the studied systems has been previously observed for Fe_3O_4 NPs.[50] Moreover, as has already been stated, the net magnetization of the $NiFe_2O_4$@DMSA systems is slightly lower compared to the as-prepared ones; thus we can conclude that small differences in these values cause significant differences in SAR values of each system. Hysteresis losses for the systems can be excluded since no significant difference arose from hysteresis loops. Magnetization measurements on samples D2 and D2@DMSA in lower magnetic fields (300 Oe and 700 Oe) are given in ESI (Fig. S4†). Considering that the thermal power dissipation is due to several types of loss processes: magnetic hysteresis loss, Neel relaxation and Brownian relaxation, and that the magnetization values, shape and size of the samples are nearly the same, the differences are attributed to the organic layer and Brownian relaxation is dominant.[51] Thus, among the two different organic layers, the larger size of the coating CTAB compared to DMSA ligand increased the SAR values.

To the best of our knowledge, there are only a few studies on hyperthermic effects and the calculation of SAR values for $NiFe_2O_4$ nanoparticles in the literature. These studies were carried out under different experimental conditions and thus straightforward comparison is not possible; for 5 nm $NiFe_2O_4$ the SAR value found is 1.85 W g^{-1} (f = 300 kHz and H_o = 98 Oe)[52] while the influence of frequencies (30–210 kHz) at a fixed applied field (80 Oe) for 28.4 nm $NiFe_2O_4$ has been studied[53] and the dependence of self-heating temperature on applied magnetic fields (60–160 Oe) at a fixed frequency (40 kHz) for 35 nm $NiFe_2O_4$ has been given by Bae *et al.*[54]

4. Conclusions

Monodispersed $NiFe_2O_4$ NPs of similar sizes (9.7 and 9.0 nm) have been effectively synthesized when OAm is applied in a triple role or also in the presence of a typical non-polar solvent (diphenyl ether) with normalized magnetization values (50.1 and 53.5 emu g^{-1}) close to the bulk. When an extra reducing agent was applied (hydrazine) although the size (9.0 nm) and shape remained the same, the magnetization value decreased (38.8 emu g^{-1}) and is attributed to the different Fe^{2+}/Fe^{3+} distributions in the spinel. In the presence of water a different formation mechanism occurred which led to bigger nanoparticles (11.7 nm) with a decreased magnetization value (32.0 emu g^{-1}) implying a different structural mode of the spinel. Surface modification was achieved successfully through the addition of CTAB molecules and the ligand exchange procedure through the DMSA ligand as the systems showed good colloidal stability for a period of six months. The different surface modification affected both the NMR relaxometric measurements and the hyperthermia effects. In both techniques, CTAB modification demonstrated higher r_2 relaxivity (278.9 s^{-1} mM^{-1} in an NMR spectrometer at 11.7 T) and SAR values (423.4 W g^{-1} at an applied AC field with a particle concentration of 0.5 mg mL^{-1}) indicating that a larger sized coating under the same size, shape and magnetization of $NiFe_2O_4$ NPs is more effective, although further functionalization with a variety of biomolecules can be achieved with DMSA ligands.

Acknowledgements

This research has been co-financed by the European Union (European Social Fund – ESF) and Greek national funds through the Operational Program "Education and Lifelong Learning" of the National Strategic Reference Framework (NSRF) – Research Funding Program: Thales. Investing in knowledge society through the European Social Fund.

References

1 D. H. Han, H. L. Luo and Z. Yang, *J. Magn. Magn. Mater.*, 1996, **161**, 376–378.
2 A. K. Giri, K. Pellerin, W. Pongsaksawad, M. Sorescu and S. A. Majetich, *IEEE Trans. Magn.*, 2000, **36**, 3029–3031.
3 Y. Jun, J. Lee and J. Cheon, *Angew. Chem., Int. Ed.*, 2008, **47**, 5122–5135.
4 T. Neuberger, B. Schöpf, H. Hofmann, M. Hofmann and B. von Rechenberg, *J. Magn. Magn. Mater.*, 2005, **293**, 483–496.
5 R. Hergt, S. Dutz, R. Müller and M. Zeisberger, *J. Phys.: Condens. Matter*, 2006, **18**, S2919–S2934.
6 For example see: (*a*) N. Spaldin, in *Magnetic Materials: Fundamentals and Device Applications*, Cambridge University Press, Cambridge, 2003; (*b*) G. Schmid, in *Nanoparticles: From theory to application*, WILEY-VCH Verlag GmbH & Co. KGaA, Weinheim, 2010; (*c*) M. Colombo, S. Carregal-Romero, M. F. Casula, L. Gutiérrez, M. P. Morales, I. B. Böhm, J. T. Heverhagen, D. Prosperi and W. J. Parak, *Chem. Soc. Rev.*, 2012, **41**, 4306–4334.
7 For example see: (*a*) J.-t. Jang, H. Nah, J.-H. Lee, S. H. Moon, M. G. Kim and J. Cheon, *Angew. Chem., Int. Ed.*, 2009, **48**, 1234–1238; (*b*) J.-H. Lee, Y.-M. Huh, Y.-w. Jun, J.-w. Seo, J.-t. Jang, H.-T. Song, S.-j. Kim, E.-J. Cho,

H.-G. Yoon, J.-S. Suh and J. Cheon, *Nat. Med.*, 2007, **13**, 95–99; (*c*) C. Liu, B. Zou, A. J. Rondinone and Z. J. Zhang, *J. Am. Chem. Soc.*, 2000, **122**, 6263–6267.
8 N. Cordente, M. Respaud, F. Senocq, M.-J. Casanove, C. Amiens and B. Chaudret, *Nano Lett.*, 2001, **1**, 565–568.
9 C. R. Vestal and Z. J. Zhang, *J. Am. Chem. Soc.*, 2003, **125**, 9828–9833.
10 J. Salafranca, J. Gazquez, N. Pérez, A. Labarta, S. T. Pantelides, S. J. Pennycook, X. Batlle and M. Varela, *Nano Lett.*, 2012, **12**, 2499–2503.
11 K. Vamvakidis, D. Sakellari, M. Angelakeris and C. Dendrinou-Samara, *J. Nanopart. Res.*, 2013, **15**, 1743.
12 V. G. Harris, N. C. Koon, C. M. Williams, Q. Zhang, M. Abe and J. P. Kirkland, *Appl. Phys. Lett.*, 1996, **68**, 2082–2084.
13 (*a*) B. D. Cullity and C. D. Graham, in *Introduction to Magnetic Materials*, Wiley-IEEE Press, New York, 2008; (*b*) S. Sun, H. Zeng, D. B. Robinson, S. Raoux, P. M. Rice, S. X. Wang and G. Li, *J. Am. Chem. Soc.*, 2004, **126**, 273–279.
14 (*a*) J. Mohapatra, A. Mitra, D. Bahadur and M. Aslam, *CrystEngComm*, 2013, **15**, 524–532; (*b*) B. Baruwati and S. V. Manorama, *Mater. Chem. Phys.*, 2008, **112**, 631–636.
15 (*a*) M. Srivastava, S. Chaubey and A. K. Ojha, *Mater. Chem. Phys.*, 2009, **118**, 174–180; (*b*) S. Phumying, S. Labuayai, E. Swatsitang, V. Amornkitbamrung and S. Maensiri, *Mater. Res. Bull.*, 2013, **48**, 2060–2065.
16 (*a*) S. Yáñez-Vilar, M. Sánchez-Andújar, C. Gómez-Aguirre, J. Mira, M. A. Señarís-Rodríguez and S. Castro-García, *J. Solid State Chem.*, 2009, **182**, 2685–2690; (*b*) J. Wang, F. Ren, R. Yi, A. Yan, G. Qiu and X. Liu, *J. Alloys Compd.*, 2009, **479**, 791–796.
17 M. George, A. M. John, S. S. Nair, P. A. Joy and M. R. Anantharaman, *J. Magn. Magn. Mater.*, 2006, **302**, 190–195.
18 P. Sivakumar, R. Ramesh, A. Ramanand, S. Ponnusamy and C. Muthamizhchelvan, *J. Alloys Compd.*, 2013, **563**, 6–11.
19 A. Alarifi, N. M. Deraz and S. Shaban, *J. Alloys Compd.*, 2009, **486**, 501–506.
20 D. S. Jung and Y. C. Kang, *J. Magn. Magn. Mater.*, 2009, **321**, 619–623.
21 P. Sivakumar, R. Ramesh, A. Ramanand, S. Ponnusamy and C. Muthamizhchelvan, *Mater. Res. Bull.*, 2011, **46**, 2204–2207.
22 J. Smit and H. P. J. Wijn, in *Ferrites-Physical Properties of Ferrimagnetic Oxides in Relation to their Technical Applications*, Wiley, New York, 1959.
23 (*a*) C.-C. Huang, C.-Y. Tsai, H.-S. Sheu, K.-Y. Chuang, C.-H. Su, U.-S. Jeng, F.-Y. Cheng, C.-H. Su, H.-Y. Lei and C.-S. Yeh, *ACS Nano*, 2011, **5**, 3905–3916; (*b*) H. Fan, E. Leve, J. Gabaldon, A. Wright, R. E. Haddad and C. J. Brinker, *Adv. Mater.*, 2005, **17**, 2587–2590.
24 L. I. Cabrera, Á. Somoza, J. F. Marco, C. J. Serna and M. P. Morales, *J. Nanopart. Res.*, 2012, **14**, 873.
25 (*a*) A. G. Roca, S. Veintemillas-Verdaguer, M. Port, C. Robic, C. J. Serna and M. P. Morales, *J. Phys. Chem. B*, 2009, **113**, 7033–7039; (*b*) A. Ruiz, G. Salas, M. Calero, Y. Hernandez, A. Villanueva, F. Herranz, S. Veintemillas-Verdaguer, E. Martinez, D. F. Barber and M. P. Morales, *Acta Biomater.*, 2013, **9**, 6421–6430.
26 S. Mourdikoudis and L. M. Liz-Marzán, *Chem. Mater.*, 2013, **25**, 1465–1476.
27 L. Perez-Mirabet, E. Solano, F. Martınez-Julia, R. Guzman, J. Arbiol, T. Puig, X. Obradors, A. Pomar, R. Yanez, J. Ros and S. Ricart, *Mater. Res. Bull.*, 2013, **48**, 966–972.
28 For example see: (*a*) J. Xie, S. Peng, N. Brower, N. Pourmand, S. X. Wang and S. Sun, *Pure Appl. Chem.*, 2006, **78**, 1003–1014; (*b*) C. A. Crouse and A. R. Barron, *J. Mater. Chem.*, 2008, **18**, 4146–4153.
29 C. Salzemann, A. Brioude and M.-P. Pileni, *J. Phys. Chem. B*, 2006, **110**, 7208–7212.
30 W. Wu, Q. He and C. Jiang, *Nanoscale Res. Lett.*, 2008, **3**, 397–415.
31 H. P. Kluge and L. E. Alexander, in *X-ray Diffraction Procedure*, Wiley Inter Science, New York, 1974.
32 H. Li, H.-Z. Wu and G.-X. Xiao, *Powder Technol.*, 2010, **198**, 157–166.
33 T. Rohani Bastami, M. H. Entezari, Q. Hong Hu, S. Budi Hartono and S. Z. Qiao, *Chem. Eng. J.*, 2012, **210**, 157–165.
34 J. Coates, in *Interpretation of Infrared Spectra, A Practical Approach in Encyclopedia of Analytical Chemistry*, ed. R. A. Meyers, John Wiley & Sons Ltd, Chichester, 2000, pp. 10815–10837.
35 R. D. Waldron, *Phys. Rev.*, 1955, **99**, 1727–1735.
36 C. Kim, M. Min, Y. W. Chang, K.-H. Yoo and H. Lee, *J. Nanosci. Nanotechnol.*, 2010, **10**, 233–239.
37 (*a*) M. A. Willard, Y. Nakamura, D. E. Laughlin and M. E. McHenry, *J. Am. Ceram. Soc.*, 1999, **82**, 3342–3346; (*b*) P. P. Kirichok, *Fizika*, 1968, **11**, 67–71.
38 T. N. Shendruk, R. D. Desautels, B. W. Southern and J. van Lierop, *Nanotechnology*, 2007, **18**, 455704.
39 (*a*) Y. Tian, B. Yu, X. Li and K. Li, *J. Mater. Chem.*, 2011, **21**, 2476–2481; (*b*) S. Vaidya, P. Rastogi, S. Agarwal, S. K. Gupta, T. Ahmad, A. M. Antonelli Jr., K. V. Ramanujachary, S. E. Lofland and A. K. Ganguli, *J. Phys. Chem. C*, 2008, **112**, 12610–12615.
40 For example see: (*a*) A. Repko, D. Nižňanský and J. Poltierová-Vejpravová, *J. Nanopart. Res.*, 2011, **13**, 5021–5031; (*b*) Z. P. Chen, Y. Zhang, K. Xu, R. Z. Xu, J. W. Liu and N. Gu, *J. Nanosci. Nanotechnol.*, 2008, **8**, 6260–6265.
41 (*a*) M. Song, Y. Zhang, S. Hu, L. Song, J. Dong, Z. Chen and N. Gu, *Colloids Surf. A: Physicochem. Eng. Aspects*, 2012, **408**, 114–121; (*b*) J. Aldana, N. Lavelle, Y. Wang and X. Peng, *J. Am. Chem. Soc.*, 2005, **127**, 2496–2504; (*c*) S. K. Basiruddin, A. Saha, N. Pradhan and N. R. Jana, *J. Phys. Chem. C*, 2010, **114**, 11009–11017.
42 C. Sun, J. S. H. Lee and M. Zhang, *Adv. Drug Delivery Rev.*, 2008, **60**, 1252–1265.
43 (*a*) A. J. Villaraza, A. Bumb and M. W. Brechbiel, *Chem. Rev.*, 2010, **110**, 2921–2959; (*b*) Y. X. Wang, S. M. Hussain and G. P. Krestin, *Eur. Radiol.*, 2001, **11**, 2319–2331; (*c*) H. Ai, *Adv. Drug Delivery Rev.*, 2011, **63**, 772–788.

44 S. H. Koenig and K. E. Kellar, *Magn. Reson. Med.*, 1995, **34**, 227–233.
45 S. L. C. Pinho, G. A. Pereira, P. Voisin, J. Kassem, V. Bouchaud, L. Etienne, J. A. Peters, L. Carlos, S. Mornet, C. F. G. C. Geraldes, J. Rocha and M.-H. Delville, *ACS Nano*, 2010, **4**, 5339–5349.
46 (*a*) J. Qin, S. Laurent, Y. S. Jo, A. Roch, M. Mikhaylova, Z. M. Bhujwalla, R. N. Muller and M. Muhammed, *Adv. Mater.*, 2007, **19**, 1874–1878; (*b*) H. Yang, H. Zhou, C. Zhang, X. Li, H. Hu, H. Wu and S. Yang, *Dalton Trans.*, 2011, **40**, 3616–3621; (*c*) H. Ai, C. Flask, B. Weinberg, X. Shuai, M. D. Pagel, D. Farrell, J. Duerk and J. Gao, *Adv. Mater.*, 2005, **17**, 1949–1952.
47 A. Jordan, P. Wust, H. Fahlin, W. John, A. Hinz and R. Felix, *Int. J. Hyperthermia*, 1993, **9**, 51–68.
48 (*a*) B. A. Bornstein, P. S. Zouranjian, J. L. Hansen, S. M. Fraser, L. A. Gelwan, B. A. Teicher and G. K. Svensson, *Int. J. Radiat. Oncol.*, 1993, **25**, 79–85; (*b*) V. M. Khot, A. B. Salunkhe, N. D. Thorat, R. S. Ningthoujam and S. H. Pawar, *Dalton Trans.*, 2013, **42**, 1249–1258.
49 S. Purushotham, P. E. J. Chang, H. Rumpel, I. H. C. Kee, R. T. H. Ng, P. K. H. Chow, C. K. Tan and R. V. Ramanujan, *Nanotechnology*, 2009, **20**, 305101.
50 (*a*) Y. Pineiro-Redondo, M. Bañobre-López, I. Pardinas-Blanco, G. Goya, M. A. López-Quintela and J. Rivas, *Nanoscale Res. Lett.*, 2011, **6**, 383; (*b*) K. D. Bakoglidis, K. Simeonidis, D. Sakellari, G. Stefanou and M. Angelakeris, *IEEE Trans. Magn.*, 2012, **48**, 1320–1323.
51 P. Crespo, P. de la Presa, P. Marín, M. Multigner, J. M. Alonso, G. Rivero, F. Yndurain, J. M. González-Calbet and A. Hernando, *J. Phys.: Condens. Matter*, 2013, **25**, 484006.
52 O. V. Yelenich, S. O. Solopan, T. V. Kolodiazhnyi, V. V. Dzyublyuk, A. I. Tovstolytkin and A. G. Belous, *Solid State Sci.*, 2013, **20**, 115–119.
53 S. Bae, S. W. Lee, A. Hirukawa, Y. Takemura, Y. H. Jo and S. G. Lee, *IEEE T. Nanotechnol.*, 2009, **8**, 86–94.
54 S. Bae, S. W. Lee and Y. Takemura, *Appl. Phys. Lett.*, 2006, **89**, 252503.

